

# Homochirality in the Vicsek model: fluctuations and potential implications for cellular flocks

Hoffmann, L.A.; Giomi, L.

# Citation

Hoffmann, L. A., & Giomi, L. (2025). Homochirality in the Vicsek model: fluctuations and potential implications for cellular flocks. *Physical Review E*, 111(1). doi:10.1103/PhysRevE.111.015427

Version: Publisher's Version

License: Licensed under Article 25fa Copyright Act/Law (Amendment Taverne)

Downloaded from: <a href="https://hdl.handle.net/1887/4281840">https://hdl.handle.net/1887/4281840</a>

**Note:** To cite this publication please use the final published version (if applicable).

# Homochirality in the Vicsek model: Fluctuations and potential implications for cellular flocks

Ludwig A. Hoffmann

Instituut-Lorentz, Universiteit Leiden, P. O. Box 9506, 2300 RA Leiden, The Netherlands and John A. Paulson School of Engineering and Applied Sciences, Harvard University, Cambridge, Massachusetts 02138, USA

Luca Giomi \*\*

Instituut-Lorentz, Universiteit Leiden, P. O. Box 9506, 2300 RA Leiden, The Netherlands

(Received 28 July 2023; accepted 20 December 2024; published 23 January 2025)

Chirality is a feature of many biological systems, and much research has been focused on understanding the origin and implications of this property. Famously, sugars and amino acids found in nature are homochiral, i.e., chiral symmetry is broken and only one of the two possible chiral states is ever observed. Certain types of cells show chiral behavior, too. Understanding the origin of cellular chirality and its effect on tissues and cellular dynamics is still an open problem and subject to much (recent) research, e.g., in the context of drosophila morphogenesis. Here, we develop a simple model to describe the possible origin of homochirality in cells. Combining the Vicsek model for collective behavior with the model of Jafarpour et al. [Phys. Rev. Lett. 115, 158101 (2015)], developed to describe the emergence of molecular homochirality, we investigate how a homochiral state might have evolved in cells from an initially symmetric state without any mechanisms that explicitly break chiral symmetry. We investigate the transition to homochirality and show how the "openness" of the system as well as noise determine if and when a globally homochiral state is reached. While hypothetical and explorative in nature, our analysis may serve as a starting point for more realistic models of chirality in flocking multicellular systems.

### DOI: 10.1103/PhysRevE.111.015427

#### I. INTRODUCTION

Chirality, i.e., the property in which an object differs from its mirror image, is a common feature of many biological systems, from amino acids up to biopolymers, cells, and fully developed vertebrate and invertebrate organisms [1-3]. Most biomolecules, for instance, are either left- or right-handed (L or R for brevity), despite the reactions starting them not favoring either of the two handednesses. Thus, most amino acids are left-handed, whereas R-molecules are predominant among sugars. These small chiral molecules, in turn, serve as building blocks of larger biopolymers, thereby providing the molecular basis for a hierarchical inheritance of chirality by larger structures.

Because of its ubiquitousness in biology, the origin and the relevance of chirality has been the subject of insightful research for decades; see, e.g., Refs. [4-8] and references therein. The function of a specific handedness, if any, and the mechanism leading to chiral symmetry breaking, in particular, are still hotly debated. While chirality appears to be crucial in small biomolecules, where it was found to be linked to the function of, e.g., proteins [7], it is not always clear if and how chirality plays a role in larger structures. Thus, while certainly LR asymmetry is instrumental to the mechanics of flagella in sperm cells [9,10] and bacteria [11], its occurrence and role are not equally obvious in eukaryotic cells. Yet, an increasingly large body of experimental evidence has

recently begun to indicate that, even in this case, chirality could serve specific biophysical functions in both unicellular [7] and multicellular systems. For example, cell chirality has been shown to influence the morphogenesis of Drosophila [12], snails [13], C. elegans [14], and mammalian cells [15–19]. In vitro, a particularly compelling example of chirality and its effect in multicellular eukaryotes was reported in confined layers of spindlelike RPE1 and C2C12 cells [20], as well as in cancerous HT1080 cells, where chirality gives rise to topological edge currents, which rectify the chaotic cellular motion in the bulk [21]. In these examples, cellular chirality appears uniform across the entire monolayer—a property also known as homochirality—and its effect on the cells' collective dynamics can be accurately reproduced by postulating the existence of a chiral active stress, reflecting the forces exerted by the cells [20–22]. Yet, how homochirality originates at the cellular scale remains elusive.

A necessary step towards a satisfactory understanding of homochirality in multicellular systems consists of establishing whether LR-symmetry is *explicitly* or *spontaneously* broken, that is, whether cellular chirality is genetically programed to be always the same or if it can spontaneously arise during the lifetime of a system, as a consequence of mechanical instabilities of phenotypical switches. In spite of the enormous advances of live-cell imaging, the current experimental literature does not provide clear indications in this respect, with both scenarios being equally likely and possibly system-specific. For instance, Tee et al. reported that the actin cytoskeleton of human foreskin fibroblast (HFF), cultured in circular wells, robustly organizes in right-handed (i.e.,

<sup>\*</sup>Contact author: giomi@lorentz.leidenuniv.nl

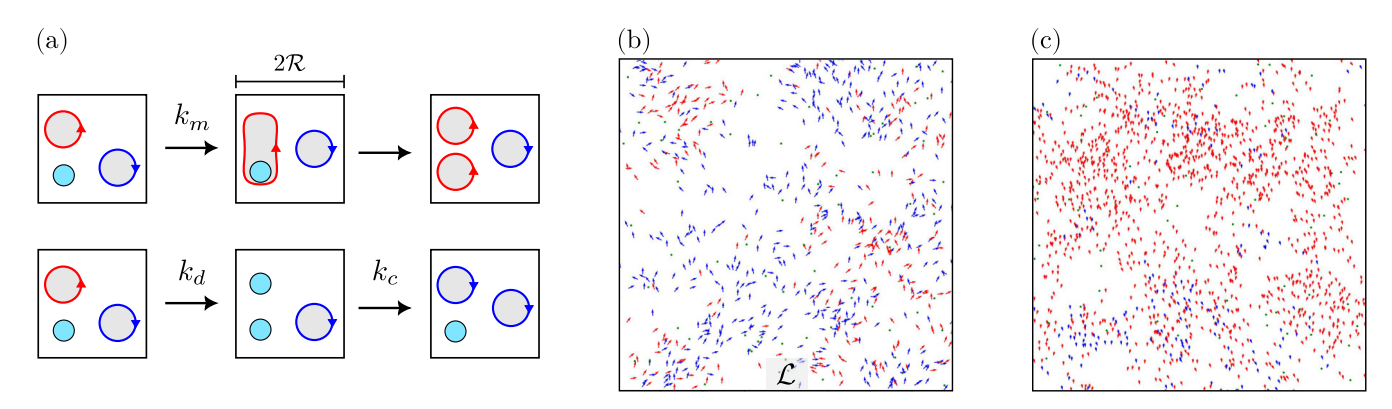


FIG. 1. Model. (a) A schematic of the reactions defined in Eqs. (1). To perform the reactions, we subdivide the total system into square boxes of height  $2\mathcal{R}$ . Left-chiral particles (blue arrow) and right-chiral particles (red arrow) can divide with the rate  $k_m$  through the consumption of nutrients (cyan dot). Our model is based on the assumption that chirality is preserved during the division process and thus inherited by daughter cells. Furthermore, they die with the rate  $k_d$  and are replaced by a nutrient, or the nutrient "spontaneously transforms" into a particle with rate  $k_c$ . Here a left-chiral particle undergoes these reactions. See the main text for a proper interpretation of the rates. (b) Snapshot of the simulations carried out in a square system of height  $\mathcal{L}$  at density  $\rho = 2$  and noise  $\rho = 0.3$ . Again, right-chiral particles are represented by blue arrows while left-chiral particles are represented by red arrows. (c) A snapshot taken for higher densities ( $\rho = 4$ ) and lower noise ( $\rho = 0.1$ ).

counterclockwise) patterns [17]. This handedness, in turn, is regulated by  $\alpha$ -actinin-1 and could be reversed only upon overexpressing the latter. In this study, the overexpression of  $\alpha$ -actinin-1 was artificially induced, but one cannot exclude that similar effects could occur spontaneously as a consequence of transcriptional switches. Because the cytoskeleton is shared between the mother and daughter cell upon division, this scenario could imply—so far only hypothetically—an inheritance of chirality from mother to daughter. In Ref. [23], conversely, Drosophila cells treated with Pak3 were observed to support both right- and left-handed traveling waves at the periphery of the cells' lamellipodium. Whether this further example of cytoskeletal handedness is sufficiently robust to be inherited upon division is, however, presently unknown. A right-handed homochirality was also found in HT1080 fibrosarcoma cells confined within fibronectin-coated strips [21], but not in a more recent in vivo study of metastatic invasion [24], thus supporting the hypothesis that cellular chirality could be phenotype-dependent and possibly change across a cell's lifecycle.

To make progress through the seemingly endless complexity of this problem, in this article we restrict our attention to a single scenario, corresponding to the case in which cellular chirality consists of an inheritable trait, which cells can transfer to each other upon division, while flocking in an open environment. This construction relies on the fundamental assumptions that cellular chirality is phenotype-dependent, hence sensitive to mechanical and biochemical cues from the cells' microenvironment, and physically encoded in the cell structure—e.g., the cytoskeleton or the spatial arrangement of the internal organelles—so to be conserved during mitotis [Fig. 1(a)]. We stress that neither one of these assumptions is confirmed by the existing experimental literature. The picture investigated here is, therefore, entirely hypothetical. Yet, by unraveling the phenomenology entailed in these assumptions, we hope to provide signatures that experiments can later confirm or disprove. Starting from a minimal model based on two reaction equations coupled with the Vicsek model [25], we show that noise breaks LR symmetry already at the cellular scale, and the system can reach a homochiral state from an initially racemic one. We numerically investigate if and how the presence of activity and alignment interactions influences the transition to homochirality from a racemic state. We find that, for specific choices of parameters, the system is guaranteed to reach a homochiral state in a finite time. While the system is in a mixed state, hence away from homochirality, we find large fluctuations of the number density and the local chirality. Furthermore, we observe that like-chiral cells are more strongly correlated than cells of opposite chirality, even though there is no explicit interaction term favoring one over the other. Finally, we find that the time a given system takes to transition to homochirality follows a long-tail distribution, with mean and standard deviation being of the same order of magnitude.

This article is organized as follows. In Sec. II, we present our model in more detail. In Secs. III and IV, on the other hand, we explore two possible regimes of the model, where the evolutionary and spatial dynamics are indirectly or directly coupled. We identify the conditions for which the system transitions from a racemic to a homochiral state, and we reconstruct the statistics of spatial fluctuations and heterogeneities. In Sec. V, we conclude this article with a brief discussion of some potential applications, for example in the context of population dynamics and genetic drift.

#### II. MODEL

We model cells as self-propelled particles with aligning interactions, and whose dynamics is governed by the classic Vicsek model [25]. To account for chirality, we follow a classic approach pioneered by Frank [4] and recently extended by Jafarpour *et al.* to explain the emergence of homochiral states in racemic mixtures of left and right (L and R) molecules [8,26]. This model assumes the existence of two possible chiralities, i.e., L and R, and a solvent—denoted with S—which can fill the space left by a cell after its death and replenish the cell layer with nutrients. These processes occur by means of

the following reactions:

$$R + S \xrightarrow{k_m} 2R$$
,  $L + S \xrightarrow{k_m} 2L$ , (1a)

$$R \underset{k_r}{\overset{k_d}{\rightleftharpoons}} S, \quad L \underset{k_r}{\overset{k_d}{\rightleftharpoons}} S.$$
 (1b)

The first two equations, Eqs. (1a), describe cell division: a cell with given chirality uptakes nutrients from the solvent and divides into two cells having the same chirality with a rate  $k_m$ . The second set of equations, Eqs. (1b), contain a forward and a backward reaction. The former, occurring with rate  $k_d$ , accounts for the death of a cell and its extrusion from the monolayer (apoptosis), after which the void left by the cell is replenished with solvent. The backward reaction, occurring with rate  $k_c$ , describes instead cells entering the monolayer from an external reservoir and replacing part of the solvent in the process. Thus, the reaction rate  $k_c$  encodes the "openness" of the cell layer, that is, its propensity to recruit cells from outside a specific region of interest or from another layer situated above or below. If the rate vanishes, the monolayer is closed and no cells can enter, while if the rate is positive, there is a nonvanishing flux of cells into the monolayer. Our model relies then on three nontrivial reaction rates:  $k_m$  (cell division),  $k_d$  (cell death), and  $k_c$  (cell influx). Note also that all reactions are symmetric for left and right chirality, i.e., there is no explicit symmetry breaking. While undoubtedly simplistic when compared to the actual life cycle of a cell embedded in a monolayer, these reactions allow us to account for two fundamental cellular processes, such as division and apoptosis, while rendering the problem tractable, by guaranteeing that the total number of cells and solvent particles, i.e.,  $N = N_R + N_L + N_S$ , is conserved. Moreover, while originating in the realm of chiral systems, Eqs. (1) could potentially describe the inheritance of any trait in a community of cells (or other active particles) that divide, die, and enter and exit an open environment. Some of our results can be thought of as generic of cellular flocks, whether chiral or achiral.

Cellular motion is described in terms of the classic Vicsek model [25] (see also Refs. [27–29] for reviews). Each cell is characterized by a position  $\mathbf{r}_i$ , a velocity  $\mathbf{v}_i = v_0(\cos\theta_i, \sin\theta_i)$ , with  $v_0$  a constant, and a chirality  $\chi_i$ , and it evolves in time according to the following set of recursion relations:

$$\mathbf{r}_i(t+1) = \mathbf{r}_i(t) + \mathbf{v}_i(t), \tag{2a}$$

$$\theta_i(t+1) = \operatorname{Arg}\left[\sum_j C_{ij}(t) \boldsymbol{v}_j(t)\right] + (1 - 2\delta_{\chi_i,L}) \Omega + \xi_i(t).$$
(2b)

Here,  $C_{ij}(t)$  is the connectivity matrix whose entries are  $C_{ij}(t) = 1$  if  $|\mathbf{r}_i(t) - \mathbf{r}_j(t)| < \mathcal{R}$ , with  $\mathcal{R}$  a constant interaction radius, and  $C_{ij}(t) = 0$  if  $|\mathbf{r}_i(t) - \mathbf{r}_j(t)| > \mathcal{R}$ . The second term in Eq. (2b) describes a chirality-dependent rotation of a given particle, i.e.,  $+\Omega$  for right-handed and  $-\Omega$  for left-handed cells. Finally,  $\xi_i(t)$  is a Gaussian-distributed random number with zero mean,  $\langle \xi_i \rangle = 0$ , and finite standard deviation,  $\sqrt{\langle \xi_i^2 \rangle} = \eta$ . Thus, the first two terms on the right-hand side of Eq. (2b) align the direction of motion of the ith cell with those of its neighbors, which in turn can process at the rate

 $\pm\Omega$  depending on the chirality of the cells. The third term, on the other hand, introduces a random rotation whose effect is to disturb such an alignment mechanism, thereby favoring isotropy across the flock. The relative importance of these two effects is determined by the constant  $\eta$ , which, in our construction, varies in the range  $0 < \eta < 1$ . If  $\eta$  is sufficiently small and the density of particles is sufficiently large, the system described by Eqs. (2) undergoes a discontinuous phase transition from a disordered to a flocking state, where all the agents persistently move in the same direction. We stress that, unlike cells, the agents comprising our model are pointlike and are, therefore, not subject to steric repulsion. The latter is known to produce large density fluctuations at the macroscopic scale (see, e.g., Ref. [29]), but it is not expected to qualitatively change the inheritance of chirality at the scale R, which, for all practical purposes, can be treated as the average cell size [30,31].

The reactions in Eqs. (1) are implemented via the Gillespie algorithm [32,33] and coupled with the dynamics described by Eqs. (2) using the following strategy. After each time step of the Vicsek model, we divide the total system into boxes of area  $(2\mathcal{R})^2$  and in each of these boxes we run m steps of the Gillespie algorithm. After updating the population in each box, we perform another time step of the Vicsek model. Our in silico cell monolayer inhabits a square box of size  $\mathcal{L}$  with a periodic boundary and, at t = 0, consists solely of one L and one R cell, with random positions and orientations. At a given density  $\rho$  there are then  $N_S(t=0) = \rho \mathcal{L}^2$  solvent particles. Thus, the total number of agents, including both cells and solvent particles, for a given density  $\rho$  is given by  $N = \rho \mathcal{L}^2 + 2$ , which, as explained above, is conserved and constant in time by construction. We fix lengthscales by setting the interaction radius to unity,  $\mathcal{R} = 1$ . In these units, we set  $k_d = 10$  and define  $\tilde{k}_m = k_m/k_d$  and  $\tilde{k}_c = k_c/k_d$ . In the following, we will always work with the rescaled rates, but we drop the tilde. The effect of varying the other model parameters will be investigated below. In Figs. 1(b) and 1(c) we show a snapshot of the simulations at different densities and values of  $N_L/N_R$ . While the global alignment in Fig. 1(b) is low, for higher values of density and lower values of noise almost all cells have the same orientation, see Fig. 1(c). We color L cells in red and R cells in blue. Note that the configuration shown in Fig. 1(c) is considerably closer to homochirality than that shown in Fig. 1(b), with  $N_L \gg N_R$ . The question of whether the density and flocking have an effect on the appearance of homochirality, or the mean time until this state is reached, will be discussed below.

#### III. $\Omega = 0$ CASE

To explore how homochirality is progressively established across the cellular flocks, we first investigate the case in which Eqs. (1) and (2) are not *explicitly* coupled, thus  $\Omega=0$ . In this case, chirality does not directly affect the motion of individual cells and the interplay between the evolutionary and spatial dynamics occurs solely at the level of *mixing*. The  $\Omega \neq 0$  will be discussed instead in Sec. IV. As we will see, the system is guaranteed to reach a homochiral state only if rate  $k_c$  vanishes. Therefore, as we are interested in the transition to homochirality, we afterwards set  $k_c=0$  and instead investigate the time

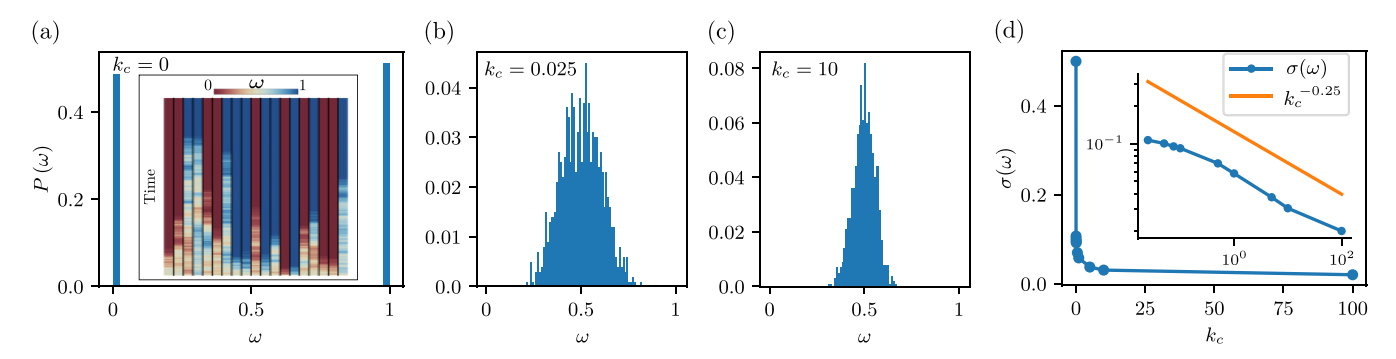


FIG. 2. Distributions of global order parameter. (a) Probability distribution  $P(\omega)$  of the order parameter  $\omega$  for vanishing rate  $k_c$ . The system is guaranteed to evolve to a homochiral state, thus  $\omega=0$  and 1 both occur with a probability of about 50%. The inset represents the time evolution of the order parameter for 20 independent runs. Each of the columns is an independent run, and time increases in the positive y-direction. The color code is according to the legend at the top, i.e.,  $\omega=0$  (homochirality of right particles) is red,  $\omega=1$  (homochirality of left particles) is blue, and the racemic state  $\omega=0.5$  is white. Every systems is initialized in a state with  $\omega=0.5$ . The order parameter can be seen to fluctuate in time, but eventually all systems evolve to one of the two homochiral states. (b) Probability distribution of the order parameter for  $k_c=0.025$ . (c) Distribution for  $k_c=10$ . To obtain each of the histograms, we measure the order parameter of the system after a certain number of time steps, where the system has on average reached a stationary state, and we average over 1000 independent runs. (d) We plot the standard deviation  $\sigma(\omega)$  of the distribution  $P(\omega)$  as a function of the reaction rate  $k_c$ . We find that the curve is well approximated by a power-law decay with exponent -0.25 [see the inset for the log-log plot of standard deviation  $\sigma(\omega)$  over  $\sigma(\omega)$ . Simulation parameters:  $\sigma(\omega)$  and  $\sigma(\omega)$  over  $\sigma$ 

it takes a given system on average to reach the homochiral state. We investigate how varying different model parameters speeds up or slows down the transition time.

#### A. Global properties of open cell layers

As mentioned in Sec. II, we interpret  $k_c$  as the rate at which new cells of either chirality are introduced into the system, but not as a result of cell division. This can occur, for instance, in open cell monolayers, when a cell enters a specific region of interest, thereby replacing (consuming) previously present nutrients, or in multilayered structures, when a cell moves from one layer to another, i.e., both processes cause a nonvanishing flux of cells into the system. This is assumed to be equally likely for cells of either chirality, therefore guaranteeing that LR symmetry is not explicitly broken. Global chirality can be identified starting from the order parameter

$$\omega = \frac{N_L}{N_L + N_R} \in [0, 1],\tag{3}$$

such that  $\omega = 1$  if all particles are L,  $\omega = 0$  if all particles are R, and  $\omega = 0.5$  in the case of a racemic mixture of L and R. We now consider the probability distribution of  $\omega$  after a given number of time steps of Eqs. (2), when the average of many independent runs has approximately reached a steady state. To obtain the probability distribution, we record the order parameter at this time for 10<sup>3</sup> independent simulations. The resulting distributions are shown in Fig. 2 for some values of  $k_c$ . If  $k_c$  vanishes, we find a bimodal probability distribution which takes nonvanishing values only at the homochiral states  $\omega = 0$  and 1; see Fig. 2(a). That is, regardless of the specific rates of division and apoptosis, the monolayer always converges within a finite time to a homochiral state, which is equally likely to be L or R. The time evolution of the order parameter for some of the runs is presented in the inset. As can be seen, the order parameter heavily fluctuates initially, but once a system has evolved into a homochiral state, it

remains in this state. This reflects the fact that, for  $k_c = 0$ , once  $N_L = 0$ , new L cells cannot be created from the reactions Eqs. (1). The only reactions occurring in the  $N_L = 0$  case are cell division and death of R cells, and similarly for  $N_R = 0$ . Thus, the homochiral states are a fixed point of the reactions if  $k_c = 0$ .

If the creation rate is finite, however, the system is not guaranteed to reach a homochiral state. Indeed, we find that already for small  $k_c$  values the probability distribution changes dramatically, with the distribution being peaked at the racemic state  $\omega=0.5$  [see Fig. 2(b) for  $k_c=0.025$ ] and the monolayer never converging to a homochiral state. As  $k_c$  increases, the width of the probability distribution decreases rapidly, and for large  $k_c$  values the distribution is sharply peaked around  $\omega=0.5$  [see Fig. 2(c) for  $k_c=10$ ]. To quantify this behavior, we computed the standard deviation  $\sigma(\omega)$  of the distributions as a function of the rate  $k_c$  over four orders of magnitude. We find that  $\sigma(\omega) \sim k_c^{-1/4}$ ; see Fig. 2(d). Lastly, note that the distribution is symmetric for all  $k_c$  values, reflecting that none of the mechanisms entailed by Eqs. (1) and (2) explicitly breaks LR symmetry. The average order parameter is, therefore, always  $\langle \omega \rangle = 0.5$ .

#### B. Spatial fluctuations

In the previous section, we discussed the probability distribution of the chiral order parameter  $\omega$  across the entire system. As already evident from the simulations of the snapshots in Figs. 1(b) and 1(c), neither  $\omega$  nor the cell number density are uniform across the monolayer, but they vary greatly in space. Such an inhomogeneity originates from the anisotropy introduced through the alignment interaction, and it is enhanced by the large density fluctuations that characterize the Vicsek model.

To investigate how the order parameter varies in space, we choose  $k_c = 0.025$  as an example and consider one scenario characterized by a relatively large noise and small density

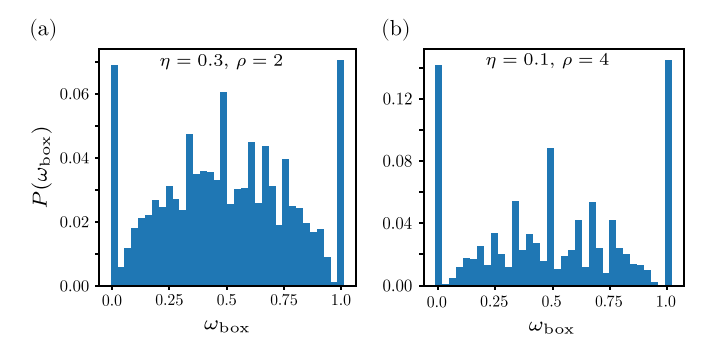


FIG. 3. Distributions of local order parameter. We measure the local order parameter  $\omega_{\rm box}$ , which is the order parameter in each of the square boxes of height  $2\mathcal{R}$ . Per system there are  $(\mathcal{L}/2\mathcal{R})^2=100$  boxes. To obtain the histograms shown here, we average over 1000 independent runs. If a box is empty, the order parameter is not well defined and we do not include it in the histogram. (a) The probability distribution for noise  $\eta=0.3$  and density  $\rho=2$ . (b) The probability distribution for noise  $\eta=0.1$  and density  $\rho=4$ . Simulation parameters:  $k_c=0.025, k_m=5, v_0=0.4, m=2$ .

(i.e.,  $\eta = 0.3$  and  $\rho = 2$ ), and another one where noise is small and density large (i.e.,  $\eta = 0.1$  and  $\rho = 4$ ). The latter is deep in the flocking regime [see the snapshot in Fig. 1(c)], while for the former the overall alignment of the cells is weaker [see the snapshot in Fig. 1(b)]. The outcome of this analysis is summarized by the histograms in Figs. 3 and 4, which we constructed as follows. At the end of each run, we measure the order parameter  $\omega_{\rm box}$  in every box of size  ${\cal R}$  of the system. We only include the order parameter in the histogram if this box is not empty, i.e., if it contains at least one L or R cell, such that the order parameter is welldefined. The histogram is then obtained from averaging over all independent runs. We find that this probability distribution is strongly peaked around  $\omega_{\text{box}} = 0$  and 1, and that there is another maximum at  $\omega_{\text{box}} = 0.5$ . The relatively nonmonotonic structure of the distribution can be explained by some values of  $\omega_{\text{box}} = 0$  being much more likely to occur if they are rational numbers for ratios of a small number of cells. This is particularly evident for small densities where only a few particles are present in some boxes. However, in either case we find the general trend of the distribution decreasing away from  $\omega_{\text{box}} = 0.5$ , and then strongly increasing at the edges. A noticeable difference between the two cases shown in Fig. 3 is that for higher densities and lower noises, the relative frequency of the homochiral state is much greater. We have also considered an intermediate state of low noise and density ( $\eta = 0.1$  and  $\rho = 2$ ) (not shown), and we did not find a significant difference from the histogram in Fig. 3(a).

In Figs. 4(a) and 4(b) we present the probability distribution of the field  $n_R$ , defined as the number of R cells in a given box. As the distributions of L and R cells are identical, we only show one of the two. Again, we consider the average over independent runs at a fixed time where the average over the whole system has reached a steady state to find the probability distributions. Note that if all cells were distributed homogeneously in space,  $\langle n \rangle = (2\mathcal{R})^2 \rho$ . We normalize the number of cells by this number and write the renormalized quantities with a tilde, i.e.,  $\tilde{n}_R = n_R/\langle n \rangle$ . For  $k_c = 0$ , i.e., if

the system is homochiral, there is about a 50% probability that its entire population consists of L cells, thus  $P(\tilde{n}_R = 0) \approx 0.5$ [inset in Fig. 4(a)]. Since the probability distribution of  $\tilde{n}_R$ is trivial in this case, we now consider only the systems that evolve to R homochirality. The distribution of  $\tilde{n}_R$  is rather broad; see Fig. 4(a), with a mean of  $\langle \tilde{n}_R \rangle \approx 0.9$  cells per box with relative fluctuations of  $\sigma(\tilde{n}_R)/\langle \tilde{n}_R \rangle \approx 0.62$ , where  $\sigma(\tilde{n}_R)$  is the standard deviation of the distribution. Note that the distribution peaks at  $\tilde{n}_R = 0.75$  and decreases for both smaller and larger values. If we consider the total number of cells, without regard for their chirality, that is,  $\tilde{n} = \tilde{n}_R + \tilde{n}_L$ , we find the distribution shown in Fig. 4(b). It is essentially identical to the one for R cells (after removing the subset of systems that evolved to L homochirality), reflecting the fact that, after a monolayer has reached a homochiral state, cells are either all R or all L, thus the distribution of the number densities of the two subpopulations is equal to the distribution of the entire population. This is markedly different for nonvanishing  $k_c$ . Again, we choose  $k_c = 0.025$  as an example. The most likely case now is to encounter a box that contains no R cells and the distribution is monotonically decreasing for increasing  $\tilde{n}_R$ ; see Fig. 4(c). The average  $\langle \tilde{n}_R \rangle \approx 0.46$  is about half the previous average value (reflecting that the mean global order parameter is  $\omega = 0.5$ ), but the distribution is much wider, with the standard deviation almost being equal to the mean,  $\sigma(\tilde{n}_R)/\langle \tilde{n}_R \rangle \approx 0.99$ . Thus, fluctuations are very large. The distribution for the total number of cells in this case [Fig. 4(d)] is similar to that for vanishing rate  $k_c$ , with  $\langle \tilde{n} \rangle \approx 0.9$  and  $\sigma(\tilde{n})/\langle \tilde{n} \rangle \approx 0.75$ . However, the distributions of  $\tilde{n}$  and  $\tilde{n}_R$  (or, equivalently, of  $\tilde{n}_L$ ) are now different, as can be seen by comparing Figs. 4(c) and 4(d). With increasing  $k_c$ , the distribution preserves its structure, but  $\langle \tilde{n}_R \rangle$  slightly increases (to  $\langle \tilde{n}_R \rangle \approx 3.7$  for  $k_c = 10$ ), while the relative fluctuations slightly decrease [see the inset of Fig. 4(c)]. Mean and relative fluctuations for the total number of cells  $\tilde{n}$  remains constant. For  $k_c = 0.025$ , but higher density and lower noise ( $\rho = 4$  and  $\eta = 0.1$  compared to  $\rho = 2$  and  $\eta = 0.3$  as before), the distribution becomes less broad, with  $\langle \tilde{n}_R \rangle \approx 0.84$  and  $\langle \tilde{n} \rangle \approx 0.61$ , but its mean and structure do not change much.

To complete our analysis of spatial fluctuations in model cellular flocks, we look at the number density correlation functions, i.e.,  $C_{XY} = \langle n_X(\mathbf{r}) n_Y(\mathbf{r}') \rangle$ , where X and Y are any combination of R and L. This is shown for two different  $k_c$  values, i.e.,  $k_c = 0.025$  and 10, in Figs. 4(e) and 4(f), respectively. For  $k_c = 0.025$ , we find that, whether R or L, like-chiral cells are more strongly correlated in space than cells of opposite chirality, even at long distances; see Fig. 4(e). Furthermore, the correlation functions roughly follow a power-law decay, with the exponent associated with like-chiral cells being approximatively twice that of cells of opposite chirality. That is, for  $k_c = 0.025$ ,  $C_{RR} \approx C_{LL} \sim |\mathbf{r} - \mathbf{r}'|^{-0.2}$ , while  $C_{RL} \sim |\mathbf{r} - \mathbf{r}'|^{-0.11}$ ; see the inset in Fig. 4(e). For higher density and lower noise we find that the behavior is similar, with the ratio of the exponents again being about 2. For higher  $k_c$ , the two correlation functions instead overlap, with  $C_{\rm RR} \approx C_{\rm LL} \sim |r - r'|^{-0.18}$  and  $C_{\rm RL} \sim |r - r'|^{-0.16}$ ; see Fig. 4(f). Furthermore, in this case the large lengthscale behavior of the correlation functions is very similar as well.

In conclusion, our analysis revealed a large inhomogeneity in both the cell number density and chiral order parameter,

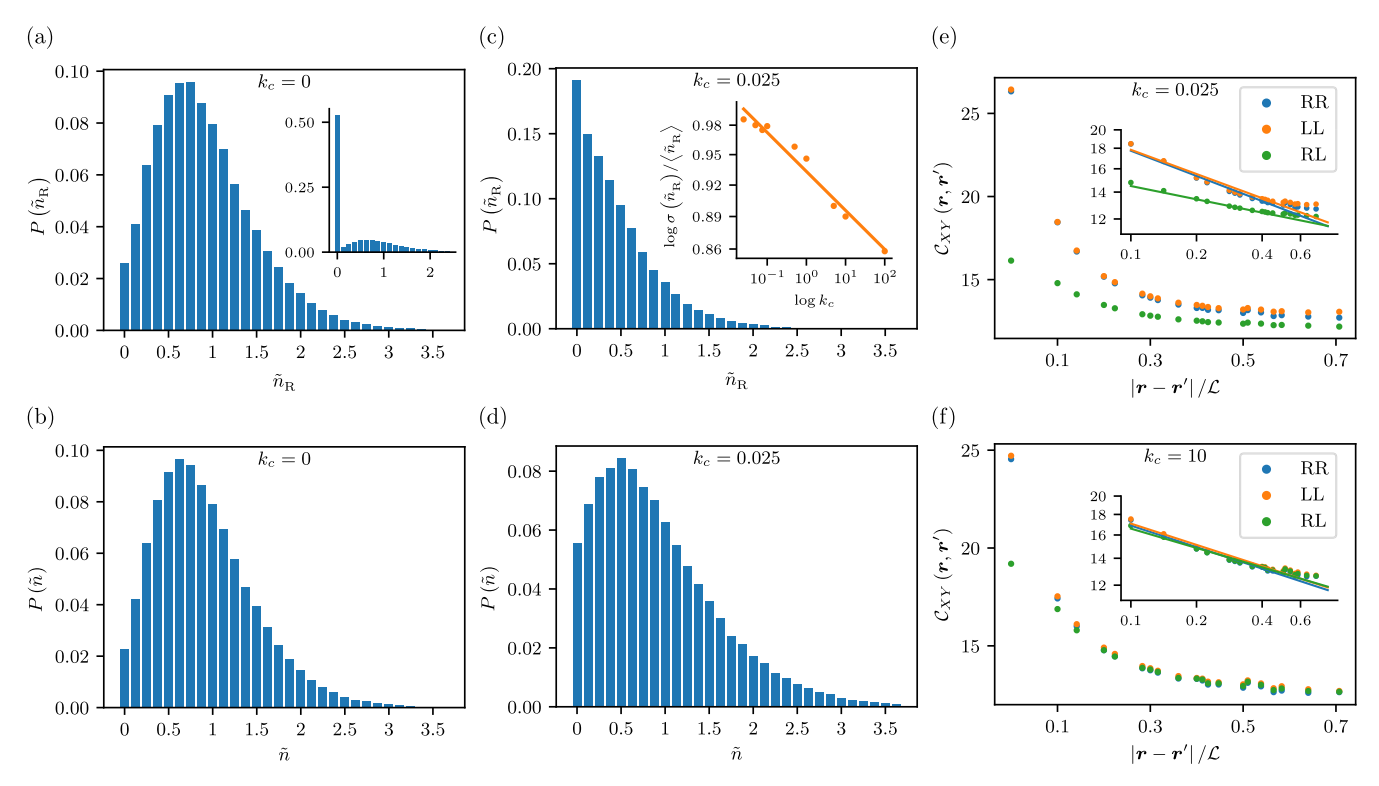


FIG. 4. Fluctuations and correlations of particles density. (a) We show the probability distribution to find a number of  $\tilde{n}_R$  right-chiral particles in a box for  $k_c=0$ . Here,  $\tilde{n}_R$  is not the total number of particles but the ratio of the number of particles over the average number of particles one would expect in a box in a homogeneous system (see the main text). Thus for  $\tilde{n}_R < 1$ , the number of particles in a box is smaller than expected in a homogeneous system, while for  $\tilde{n}_R > 1$  it is greater. The probability distribution shown here is obtained by ignoring/subtracting the cases in which the system has evolved to a left-homochiral state. The inset shows the distribution if these cases are not subtracted. The large probability of finding a box without a right-chiral particle reflects the fact that the system evolves in half of the runs to a left-homochiral where no right-chiral particles are present. (b) The probability to find a given relative total number of particles in a box. (c) The same probability distribution as in (a) but for  $k_c = 0.025$  and without subtracting the cases of left homochirality. This is because, as was shown in Fig. 2, the system virtually never evolves to a homochiral state and the systems are always mixed. The inset shows the dependence of the ratio of standard deviation over mean for the probability distribution  $P(\tilde{n}_R)$  as a function of the rate  $k_c$ . The best fit is found to be  $\sim k_c^{0.017}$ . (d) The same distribution as in (b) but for  $k_c = 0.025$ . (e) The correlation function between right-chiral particles (RR, blue), left-chiral particles (LL, orange), and left- and right-chiral particles (RL, green). The x-axis is distances measured in terms of the system size  $\mathcal{L}$ . The inset shows the same data in a log-log plot with the best fit of the linear region (in the log-log plot), namely  $0.1 < |r-r'|/\mathcal{L} < 0.5$ . (f) The same data but for  $k_c = 10$  now. Simulation parameters:  $k_m = 5$ ,  $\rho = 2$ ,  $\eta = 0.3$ ,  $v_0 = 0.4$ , m = 2.

despite chirality not affecting directly cellular motion. That is, Eqs. (2), which govern the motion as well as the orientational interactions among cells, do not distinguish between R and L. The higher spatial correlation of like-chiral cells, therefore, is indicative of an emergent feedback mechanism, which effectively enhances the interactions between the like-chiral cells.

## C. Time to homochirality

In this section, we investigate how cell motion affects the convergence to homochirality. To this end, we set  $k_c = 0$  to guarantee that either one of the two available homochiral states is reached in a finite time  $\tau$ , and we reconstruct the statistics of  $\tau$  for various parameter choices. Specifically, we again run  $10^3$  independent simulations, terminating each run once homochirality is established.

We begin this analysis with an assessment of the influence of rotational noise by varying its standard deviation  $\eta$  throughout the unit interval. We find that the mean time  $\langle \tau \rangle$  required to reach the homochiral state is significantly larger for lower

noises, quickly decreases, and eventually plateaus as noise is increased; see Fig. 5(a). Orientational noise thus facilitates the onset of homochirality by favoring the dispersion of the cells in the solvent, hence the uptake of nutrients, which is instrumental to their division. In the limiting case of vanishing noise, on the other hand, the two cells comprising the initial configuration of the system move on a straight trajectory, which quickly becomes depleted of solvent particles, thus reducing the performance of the reactions in Eqs. (1), which lead to homochirality. This effect, however, is at play only at low noise, where the dispersion of the cells in the solvent does not completely disrupt the coherence of the flock. For large  $\eta$ values, conversely, the monolayer transitions from flocking to isotropic, and the route to homochirality is equivalent to that of isolated cells. To clarify this further, we show in Fig. 5(b) the probability distributions of  $\tau$  for a few different  $\eta$  values. We find that noise has no visible influence on the mode of the distribution (i.e., the location of the peak), but it does increase the length of its tail. In conclusion, flocking slows down the convergence to homochirality by reducing the mixing of

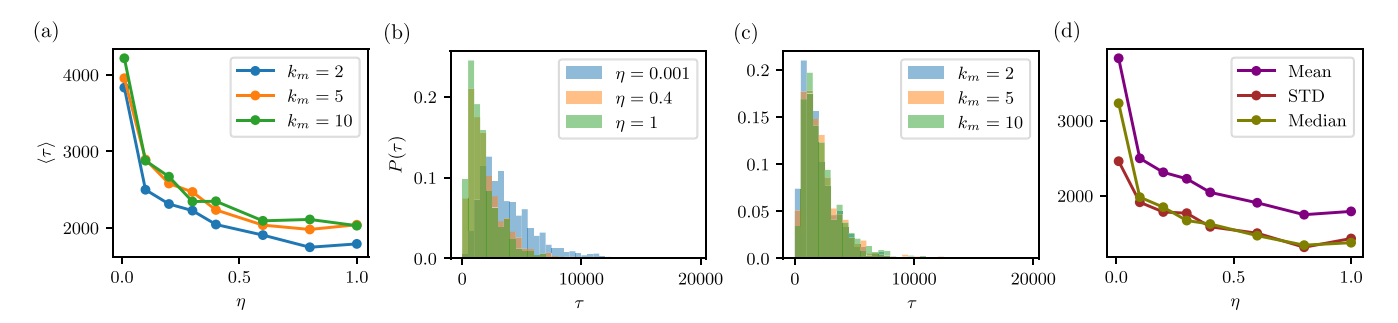


FIG. 5. Transition time for different noises and division rates. (a) The average time  $\langle \tau \rangle$  in which the system evolves for a homochiral state as a function of noise  $\eta$  for different cell division rates  $k_m$ . (b) The distribution  $P(\tau)$  of the transition time  $\tau$  found from recording  $\tau$  for 1000 independent runs for three values of noise. (c) The same distribution but now for three different division rates. (d) The mean (purple), standard deviation (STD, red), and median (olive green) of the distribution  $P(\tau)$  for different values of noise and for one division rate,  $k_m = 5$ . Simulation parameters:  $k_c = 0$ ,  $\rho = 2$ ,  $v_0 = 0.4$ , m = 2.

the cells, hence the effective biological noise. However, such an effect can be drastically reduced by introducing a small amount of orientational noise, which can restore efficient mixing without disrupting the flock.

Next, we consider different values for the cell division rate  $k_m$ . Remember that the rate  $k_m$  is defined relative to the death rate such that  $k_m > 1$  is required for a growing cell population (greater division than the death rate) and that for  $k_m < 1$  the cells in a given system will eventually all die. Surprisingly, the value of the ratio is rather irrelevant, with the mean length for  $k_m = 2$  and 10 being very similar even though in the former case the cells are dying at a rate five times higher; see Fig. 5(a). In particular, different rates show the same power-law behavior. To illustrate the similarity of the three different ratios we consider, we present in Fig. 5(c) the probability distribution for different rate ratios at a fixed noise. Indeed, they are almost indistinguishable. We find that these probability distributions are again strongly peaked at small times, but that there is a long tail with some runs taking almost five times the average time to reach homochirality. To quantify the probability distribution of the time to homochirality, we present the mean, standard deviation, and median for a fixed rate ratio  $k_m = 5$  for different noises. Note that the results for  $k_m = 2$  and 10 are almost identical. We find that all three quantities have a similar magnitude and fall off at a similar rate, with the standard deviation and mean curves overlapping while the mean is shifted by a constant factor with respect to these curves; see Fig. 5(d). All three curves follow the same power-law behavior  $\sim \eta^{-0.16(\pm 0.03)}$ .

We continue by looking at the effect of the cell speed  $v_0$ , as well as the number m of cycles of the Gillespie algorithm used to update the stochastic trajectory arising from Eqs. (1) in one time step of the Vicsek model. For both parameters we perform an analysis similar to the one for the noise presented above. Varying the speed  $v_0$ , we find that  $\tau$  decreases with increasing speed; see Fig. 6(a). The decrease is fast at low speed and slower for large  $v_0$  values. The higher the speed, the more peaked the distribution at small times. Again, we find that the standard deviation and median curves are very similar, while the mean  $\langle \tau \rangle$  changes only by a prefactor, so that all three quantities exhibit the same power-law scaling [inset in Fig. 6(a)]. A similar behavior is found when varying m. The higher the number of cycles, the faster is the convergence to

homochirality; see Fig. 6(b). The most significant difference compared with the speed  $v_0$  is that the decay is much steeper; see Fig. 6(b).

Finally, we explore the effect of density  $\rho = N/\mathcal{L}^2$  by varying the number of cells and solvent particles while keeping the magnitude of noise fixed. Together with  $\eta$ , density is a classical control parameter of the Vicsek model, which determines whether the system is in the isotropic or flocking phase. Upon increasing  $\rho$ , we find that the mean time increases slightly faster than linearly for all  $\eta$  values. Away from the smallest noise value  $\eta = 0.01$ , we do not find a significantly different behavior when varying the noise at a fixed density; see Fig. 6(c). Lastly, we note that when increasing  $\mathcal{R}$ , the mean time increases approximately linearly with R, however the value of the noise becomes less important, with the time being considerably less sensitive to changes in noise, as expected since the alignment interaction radius is increased. For these results, the cell number density is varied by changing the total number of agents, N, while keeping the size of the system,  $\mathcal{L}$ , fixed. Conversely, simultaneously increasing both N and  $\mathcal{L}$ , so as to keep  $\rho$  fixed, has the effect of progressively reducing noise, thus delaying the time to homochirality until entirely suppressing the transition in the limit  $N \to \infty$  [see Eqs. (4) and (5) in Sec. IV].

## IV. $\Omega \neq 0$ CASE

In this section, we briefly discuss the effect of including a deterministic rotation in the equation of motion, that is,  $\Omega \neq 0$  in Eq. (2b). In this case, the handedness of a given cell explicitly affects its spatial dynamics. For small  $\Omega$  values, this effect does not disrupt the onset of homochirality, and the same picture presented in Sec. III carries over, at least qualitatively. However, sufficiently large  $\Omega$  values, combined with sufficiently small values of  $\eta$ , can result in phase separation, since cells with opposite handednesses now move along divergent trajectories. Thus rotational motion effectively traps cells in a circular domain, leading to the *demixing* of the flock. An example is shown in the snapshot in Fig. 7.

This phase has previously been studied in the context of flocking of chiral active particles. These investigations were motivated by an attempt to understand the flocking behavior of chiral microswimmers such as sperm cells [34,35], bacteria

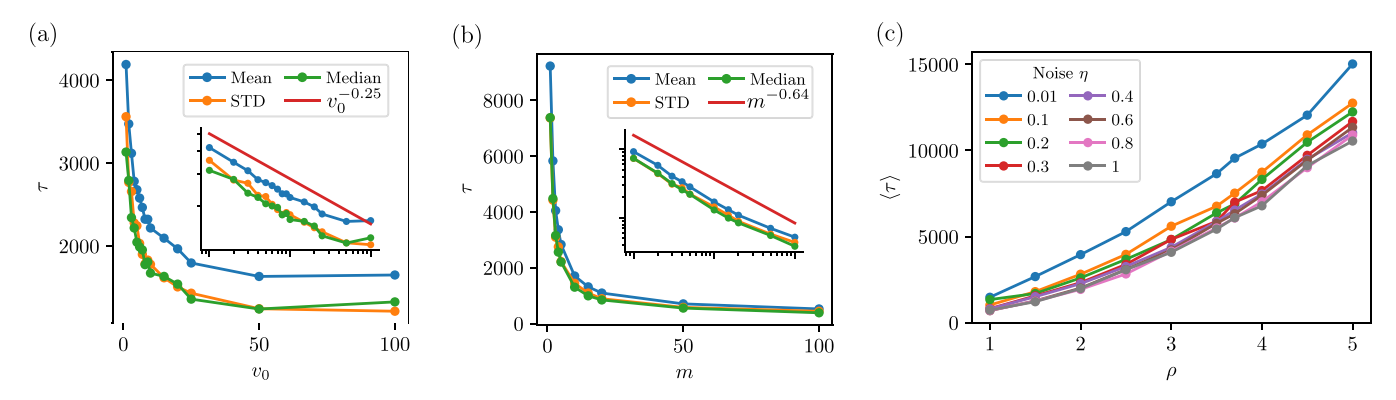


FIG. 6. Transition time for different speed and density. (a) The mean (blue), standard deviation (STD, orange), and median (green) of the distribution  $P(\tau)$  for different values of the speed  $v_0$  of the Vicsek model. The inset shows the same data but in a log-log plot, with the red line indicating the power-law decay of all three quantities  $\sim v_0^{-0.25(\pm0.02)}$ . (b) The data as in panel (a) but when varying m, the number of steps of the reactions performed during each step of the Vicsek model. Mean, standard deviation, and median now decay as  $\tau \sim m^{-0.64(\pm0.02)}$ . (c) The average time  $\langle \tau \rangle$  as a function of the density  $\rho$ . Each curve corresponds to a different value of noise  $\eta$ . Simulation parameters:  $k_c = 0$ ,  $k_m = 5$ ,  $\rho = 2$  [in panels (a) and (b)],  $v_0 = 0.4$  [in panels (b) and (c)], m = 2 [in panels (a) and (c)].

[36–40], or curved filaments [41,42]. Liebchen and Lewis [43] and Denk *et al.* [44] study a collection of self-propelled particles which all rotate with a fixed frequency  $\Omega$  and find the existence of coherently rotating flocks. When considering systems where instead half the particles have frequency  $\Omega$  and half have frequency  $-\Omega$ , curved flock trajectories (for small  $\Omega$ ) and homochiral cluster formation (for larger  $\Omega$ ) are observed [45,46]. These findings are in agreement with our numerical results.

The number of cells used in the simulations reported in Fig. 7 is unfortunately too small to exclude the possibility of finite-size effects. To mitigate this limitation and rationalize our numerical observations, we introduce here a simple continuum analog of Eqs. (1) and (2). To this end, we first review the model by Jafarpour *et al.* and discuss how the

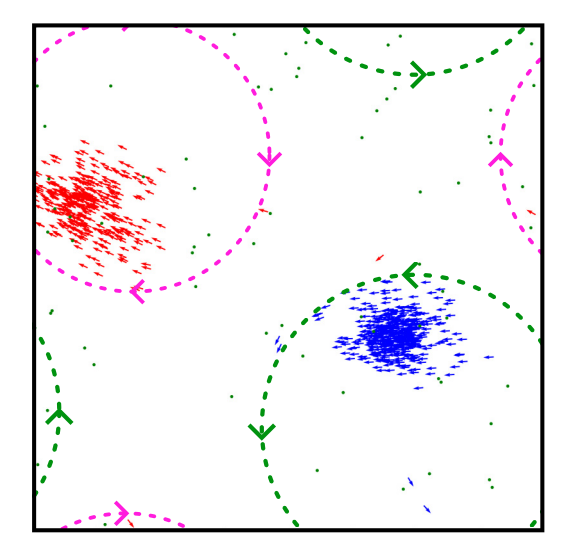


FIG. 7. Separated clusters in the presence of chiral motion. Snapshot of a system with nonvanishing deterministic rotation,  $\Omega=0.1$  and  $\eta=0.01$ . The system quickly demixes in two counterrotating vortices. Most particles are confined to the area indicated by the dashed lines, and this state is stable for long times.

mechanism presented in Refs. [8,26], used to explain the onset of molecular homochirality, combined with our findings, allows one to formulate a possible explanation of the chiral cellular flows investigated by Duclos *et al.* [20] and others [21,22]. To account for spatially extended systems, Jafarpour *et al.* coupled Eqs. (1) with a diffusive dynamics, obtaining the following reaction-diffusion equation for the space-dependent order parameter:

$$\partial_t \omega = -\frac{2V k_c k_d}{N k_m} \left( \omega - \frac{1}{2} \right) + D_0 \nabla^2 \omega + \sqrt{\frac{2k_d}{N} \omega (1 - \omega)} \zeta. \tag{4}$$

Here,  $N\gg 1$  is the number of agents—whether it be molecules, cells, or another—V is the volume of the system,  $D_0$  is a diffusion coefficient, and  $\zeta$  is Gaussian white noise of zero mean and unit variance. Both in Refs. [8,26] and here, the noise field  $\zeta$  is independent of the stochastic processes affecting the motion of the agents, but it reflects the inherent noise of the reactions governing the inheritance of chirality or other traits. Equation (4), in turn, allows a simple explanation of the origin of homochirality in the limit of vanishing  $k_c$ . If the system is not spatially extended, diffusion is irrelevant and Eq. (4) reduces to

$$\frac{d\omega}{dt} = \sqrt{\frac{2k_d}{N}\omega(1-\omega)}\,\zeta\,,\tag{5}$$

when  $k_c = 0$ . This equation has two fixed points, i.e.,  $\omega = 0$  and 1, representing the two homochiral states. Perhaps more interestingly, the right-hand side of Eq. (5) is coupled to the noise field  $\zeta$ , indicating that noise is indispensable for the onset of homochirality. As long as  $k_c = 0$ , diffusion does not change this picture, as the structure of the fixed points is not altered by the Laplacian term in Eq. (4).

To include the effect of flocking, we next couple Eq. (4) with the simplified Toner and Tu equations (see, e.g., Ref. [47]), augmented by a local rotation with angular velocity  $\Omega = \Omega e_z$ , with  $e_z$  a unit vector in the z-direction [48,49]. To couple to motion as in Eqs. (2),  $\Omega$  must in turn be an increasing function of  $\omega$  and change sign at  $\omega = 1/2$ . At the

lowest order in  $\omega$  this gives

$$\Omega = \Omega_0(2\omega - 1),\tag{6}$$

with  $\Omega_0$  a constant. Thus, taking  $k_c = 0$  in Eq. (4) and using Eq. (6) gives, after standard manipulation,

$$\partial_t \rho + \nabla \cdot (\rho \mathbf{v}) = 0, \tag{7a}$$

$$(\partial_t + \boldsymbol{v} \cdot \nabla)\Omega = D_0 \nabla^2 \Omega + \sqrt{\Omega_0^2 - \Omega^2} \, \zeta', \qquad (7b)$$

$$(\partial_t + \lambda \mathbf{v} \cdot \nabla)\mathbf{v} = (\alpha - \beta v^2)\mathbf{v} + D_1 \nabla^2 \mathbf{v} + \mathbf{\Omega} \times \mathbf{v} - \sigma \nabla \rho + \mathbf{f}, \tag{7c}$$

where  $\zeta' = \sqrt{2k_d/N} \zeta$ . Equation (7a) is the continuity equation for the cell total number, with  $\rho$  the number density, while Eq. (7b) is simply obtained upon incorporating advection in Eq. (4). Equation (7c), finally, describes flocking with average speed  $v = \sqrt{\alpha/\beta}$ . In the spirit of the Toner-Tu theory [50], one can set  $\alpha = \alpha_0(\rho - \rho_c)$ , with  $\rho_c$  a critical density and  $\beta = \beta_0 \rho$ . This guarantees the existence of a continuous phase transition from an isotropic to a flocking state when  $\rho > \rho_c$ , so that  $v = v_0 \sqrt{1 - \rho_c/\rho}$  at steady state, with  $v_0 = \sqrt{\alpha_0/\beta_0}$ . The terms proportional to  $\mathbf{v}\nabla\mathbf{v}$  and  $\nabla\rho$  represent self-advection and the ordering effect caused by possible density gradients, with  $\lambda$  and  $\sigma$  constants, whereas the aligning interactions characteristic of the Vicsek model are embodied here in a single diffusive term  $D_1 \nabla^2 v$ . Finally, the term  $\Omega \times v$  describes the persistent circular motion introduced by chirality, while f is again a white Gaussian vectorial noise field, with zero mean and variance proportional to  $\eta^2$  [49].

We stress that Eqs. (7) are not obtained from a systematic coarse-graining strategy and only aim at capturing *qualitative* aspects of the particle model embodied in Eqs. (2). A thorough analysis of Eq. (7) will be reported in a future work. Here, we restrict ourselves to elucidating the origin of phase separation in chiral flocks, as suggested by Fig. 7. First we note that, in the isotropic phase where  $\mathbf{v} = \mathbf{0}$ , Eqs. (7) reduce to Jafarpour *et al.*'s model for the case  $k_c = 0$ , thus  $\Omega = \pm \Omega_0$ , with each sign representing a specific handedness. In the flocking phase, a long-time mean-field solution of Eqs. (7) is found by assuming that cells have reached a stationary state, where diffusion is no longer prominent and the structure of the velocity field is dictated by the interplay between the effective inertial forces, originating from the rotatory motion, and compression. In this regime, Eqs. (7a) and (7c) reduce to

$$\nabla \rho \cdot \boldsymbol{v} + \rho \nabla \cdot \boldsymbol{v} = 0, \tag{8a}$$

$$\lambda \mathbf{v} \cdot \nabla \mathbf{v} - \mathbf{\Omega} \times \mathbf{v} + \sigma \nabla \rho = \mathbf{0}. \tag{8b}$$

Next, we seek a vortex solution of these equations, corresponding to the homochiral state, i.e.,  $\Omega=\pm\Omega_0$  and  $\mathbf{v}=\pm v\,\mathbf{e}_\phi$ , with  $v=v_0\sqrt{1-\rho/\rho_c}$  and  $\mathbf{e}_\phi=-\sin\phi\,\mathbf{e}_x+\cos\phi\,\mathbf{e}_y$ . Using this *ansatz* and assuming the speed v, and hence the density  $\rho$ , to be a sole function of the distance r from the center of the vortex, i.e., v=v(r), allows casting Eqs. (8) as a single differential equation of the form

$$2\Lambda^{-1}\partial_r v = \left[\left(\frac{v}{v_0}\right)^2 - 1\right]^2 \left(\frac{v}{r} - \frac{\Omega}{\lambda}\right),\tag{9}$$

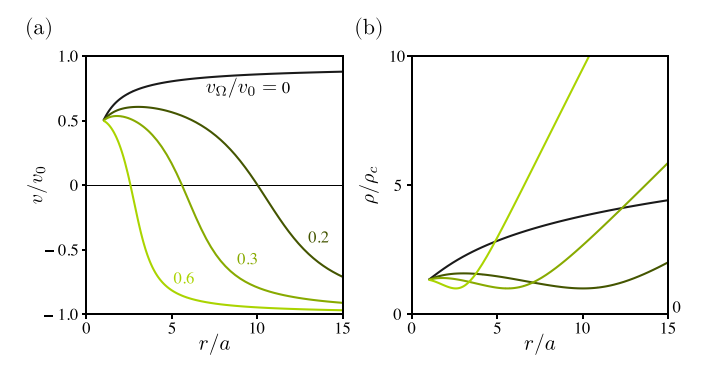


FIG. 8. Vortex structure for  $\Omega \neq 0$ . (a) The vortex speed v and (b) density  $\rho$  vs the distance from the core obtained from a numerical solutions of Eq. (9) for  $\Lambda=0$  and different values of  $v_\Omega/v_0$ , with  $v_\Omega=a\Omega$ . For finite  $v_\Omega/v_0$  values, a single homochiral vortex is mechanically unstable, as indicated by the fact that speed v changes sign at a distance  $r/a \sim v_0/v_\Omega$  from the core.

where  $\Lambda = \lambda v_0^2/(\sigma \rho_c)$ . Now, when  $\Omega_0 = 0$ , the solution of Eq. (9) is given in terms of  $\rho$  and v by

$$\frac{\rho}{\rho_c} = 1 + W \left[ \left( \frac{r}{a} \right)^{\Lambda} \right], \tag{10a}$$

$$\frac{v}{v_0} = \sqrt{1 - \frac{\rho_c}{\rho}},\tag{10b}$$

where W=W(x) is the so-called Lambert function, defined from solution of the transcendental equation  $We^W=x$ , and a is the vortex core radius [47]. This corresponds to a self-spinning vortex, whose speed vanishes at the core, increases monotonically with r/a, and eventually saturates at large distances, where  $\rho/\rho_c\approx 1+\Lambda\log(r/a)$  for  $r/a\to\infty$ , so that  $v\to v_0$  (see Fig. 8). This structure, in turn, reflects the balance between the effective *centrifugal* force caused by the self-advection, proportional to  $\lambda v^2/r$ , and the *centripetal* force, proportional to  $-\sigma \partial_r \rho$ , arising in response to the accumulation of cells away from the vortex core.

A finite  $\Omega$  value interferes with this balance by introducing an additional effective Coriolis force, proportional to  $-\Omega v$ , which acts towards establishing a rigid-body rotation, with  $v = (\Omega/\lambda)r$ . However, as is now evident from Eq. (9), the latter can lead to a steady state only in the limit  $\Lambda \to \infty$ , that is, when the speed v of the rotating flock is unbounded. Any finite  $v_0$  value, on the other hand, renders rigid body rotation unstable when  $v > v_0$ , that is, at a distance  $r/a \sim v_0/v_{\Omega}$  from the vortex core, where  $v_{\Omega} = a\Omega/\lambda$  is the inherent velocity scale introduced by chirality. This mechanism is reflected in the plots of Fig. 8, corresponding to numerical solutions of Eq. (9) for different values of the dimensionless velocity ratio  $v_{\Omega}/v_0$  and  $\Lambda=1$ . Consistent with the previous discussion, for  $v_{\Omega}/v_0 = 0$  the vortex speed plateaus to  $v_0$  at a large distance from the core. For finite  $v_{\Omega}/v_0$  values, on the other hand, v changes sign at a distance becoming shorter and shorter as  $v_{\Omega}$  increases, indicating the propensity of a single homochiral vortex to split into two counter-rotating vortices.

#### V. CONCLUSIONS

In this article, we investigated the onset of homochirality in a population of collectively moving cells by coupling the Vicsek model with reaction equations modeling cell division, death, and an influx of cells from the external environment. This model is based on the crucial assumption that cellular handedness is conserved during mitosis, so that chirality is *de facto* an inheritable trait, which cells can pass to each other across generations. This assumption, on the other hand, has never been specifically tested in experiments. The scenario investigated in this work is, therefore, entirely hypothetical.

In the absence of a direct coupling between cellular handedness and motion, we found that the system is guaranteed to evolve to a homochiral state from an initially symmetrically mixed state in finite time only if the system is closed in the sense that the reaction rate  $k_c$  vanishes. In the mixed state, we find large fluctuations of the local order parameter and the particle density around the mean value. In particular, we find that cells of the same chirality tend to be correlated more strongly in space than cells of opposite chirality. In the case in which the system evolves to a homochiral state, we showed that the transition time has a fat-tail distribution with the ratio of mean and standard deviation being of order unity. Introducing a small amount of noise in the spatial dynamics significantly decreases the mean transition time. Lastly, we found that the time decays like a power law with the speed  $v_0$  of the Vicsek model and the number of steps m of the reactions. This picture continues to hold in the presence of a weak direct coupling between chirality and motion, implemented here as a deterministic rotation in the direction of a cell's handedness. When this effect becomes dominant, however, cells split into two counter-rotating vortices, and a homochiral state can no longer be established in a finite time.

While the onset of homochirality in flocking tissues is the primary focus of this investigation, the case in which the evolutionary and spatial dynamics are not directly coupled could also serve as a toy model for the inheritance of binary traits in generic flocking systems. For example, the spatial dynamics of some types of bacteria have been successfully described using the Vicsek model (see, e.g., Refs. [28,51–54]). Our model (or a potentially slightly modified version) can therefore be used to describe the evolution of chirality, inhomogeneous phenotypes, motility, or other properties in bacterial colonies. Furthermore, bacterial colonies often consist of several interacting species, and our model can be applied to the study of the dynamics of such systems. These examples connect our model with the recent work of, for example, Refs. [55-58]. In particular, experimental realizations using bacteria colonies might be more accessible than eukaryotic cell layers.

In the context of population dynamics and genetics, the question of how traits are inherited from generation to generation is fundamental. Changes in time can be due to either natural selection (external pressures resulting in an increased fitness) or neutral processes, where changes are due to random chance. A prominent example of the latter is the change in the frequency of gene variant known as genetic drift. In particular, if a population initially contains two variants of a trait, how does their distribution evolve over time, and does one of them perhaps even go extinct (loss) such that only one variant still occurs in a population (fixation) [59-64]? For large populations, genetic drift is often negligible since fluctuations are relatively small (law of large numbers). During migration, however, genetic drift can be an important driver of diversity, for example because only a small subgroup migrates (founder effect) or because there is a frontier such that only a small subgroup of the entire population is effectively relevant [61,65-71]. A more closeup investigation of genetic drift in the presence of nontrivial spatial dynamics is therefore interesting. The model we introduced above can be a starting point for a such a study, with homochirality corresponding to fixation in this case. In a similar vein, questions about the evolution of social, rather than genetic, traits could be asked, e.g., in the context of studying the spread of languages [72].

Another opportunity for future research consists of a generalization of the model to account for nonbinary traits. This can be readily achieved by assigning each cell a trait  $T_i$ , with  $i = 1, 2, ..., N_T$ , whose kinetics is governed by reactions similar to those in Eqs. (1) and possibly affecting the dynamics of the cells. Related theoretical results have been reported in the context of active chiral cells, with the traits corresponding to different angular velocities, but without the birth-and-death dynamics characteristic of multicellular systems. Incorporating the latter into the problem would then naturally lead to the question of how the initial distribution of traits evolves in time and whether certain traits become dominant while others come to be extinct.

## ACKNOWLEDGMENTS

This work was supported by the Netherlands Organization for Scientific Research (NWO/OCW) as part of the Vidi scheme (L.A.H. and L.G.), and by the European Union via the ERC-CoGgrant HexaTissue (L.G.). L.A.H. thanks Livio Nicola Carenza, Ireth García-Aguilar, and Victor Yashunsky for valuable discussions. Part of this work was performed using the ALICE compute resources provided by Leiden University.

<sup>[1]</sup> P. Lenz, *Cell Motility*, edited by P. Lenz (Springer Science & Business Media, New York, 2008).

<sup>[2]</sup> B. Alberts, A. Johnson, J. Lewis, D. Morgan, M. Raff, K. Roberts, and P. Walter, *Molecular Biology of the Cell*, 6th ed. (Garland Science, New York, 2015).

<sup>[3]</sup> P. C. Nelson, *Biological Physics: Energy, Information, Life* (Chiliagon Science, Philadelphia, 2020).

<sup>[4]</sup> F. C. Frank, Biochim. Biophys. Acta 11, 459 (1953).

<sup>[5]</sup> S. Mason, Chem. Soc. Rev. 17, 347 (1988).

<sup>[6]</sup> D. G. Blackmond, Cold Spring Harb. Perspect. Biol. 2, a002147

<sup>[7]</sup> M. Inaki, J. Liu, and K. Matsuno, Philos. Trans. R. Soc. B 371, 20150403 (2016).

<sup>[8]</sup> F. Jafarpour, T. Biancalani, and N. Goldenfeld, Phys. Rev. E 95, 032407 (2017).

<sup>[9]</sup> J. Gray and G. Hancock, J. Exp. Biol. 32, 802 (1955).

- [10] E. Gaffney, H. Gadêlha, D. Smith, J. Blake, and J. Kirkman-Brown, Annu. Rev. Fluid Mech. 43, 501 (2011).
- [11] E. Lauga, Annu. Rev. Fluid Mech. 48, 105 (2016).
- [12] K. Taniguchi, R. Maeda, T. Ando, T. Okumura, N. Nakazawa, R. Hatori, M. Nakamura, S. Hozumi, H. Fujiwara, and K. Matsuno, Science 333, 339 (2011).
- [13] A. Davison, G. McDowell, J. Holden, H. Johnson, G. Koutsovoulos, M. Liu, P. Hulpiau, F. Van Roy, C. Wade, R. Banerjee, F. Yang, S. Chiba, J. Davey, D. Jackson, M. Levin, and M. Blaxter, Curr. Biol. 26, 654 (2016).
- [14] C. Pohl and Z. Bao, Dev. Cell 19, 402 (2010).
- [15] J. Xu, A. Van Keymeulen, N. M. Wakida, P. Carlton, M. W. Berns, and H. R. Bourne, Proc. Natl. Acad. Sci. USA 104, 9296 (2007).
- [16] L. Q. Wan, K. Ronaldson, M. Park, G. Taylor, Y. Zhang, J. M. Gimble, and G. Vunjak-Novakovic, Proc. Natl. Acad. Sci. USA 108, 12295 (2011).
- [17] Y. H. Tee, T. Shemesh, V. Thiagarajan, R. F. Hariadi, K. L. Anderson, C. Page, N. Volkmann, D. Hanein, S. Sivaramakrishnan, M. M. Kozlov, and A. D. Bershadsky, Nat. Cell Biol. 17, 445 (2015).
- [18] K. E. Worley, D. Shieh, and L. Q. Wan, Integr. Biol. 7, 580 (2015).
- [19] A. S. Chin, K. E. Worley, P. Ray, G. Kaur, J. Fan, and L. Q. Wan, Proc. Natl. Acad. Sci. USA 115, 12188 (2018).
- [20] G. Duclos, C. Blanch-Mercader, V. Yashunsky, G. Salbreux, J.-F. Joanny, J. Prost, and P. Silberzan, Nat. Phys. 14, 728 (2018).
- [21] V. Yashunsky, D. J. G. Pearce, C. Blanch-Mercader, F. Ascione, P. Silberzan, and L. Giomi, Phys. Rev. X 12, 041017 (2022).
- [22] L. A. Hoffmann, K. Schakenraad, R. M. H. Merks, and L. Giomi, Soft Matter 16, 764 (2020).
- [23] Y. Asano, A. Jiménez-Dalmaroni, T. Liverpool, M. Marchetti, L. Giomi, A. Kiger, T. Duke, and B. Baum, HFSP J. 3, 194 (2009).
- [24] O. Chepizhko, J.-M. Armengol-Collado, S. Alexander, E. Wagena, B. Weigelin, L. Giomi, P. Friedl, S. Zapperi, and C. A. M. La Porta, Proc. Natl. Acad. Sci. USA 122, e2414009121 (2025)
- [25] T. Vicsek, A. Czirók, E. Ben-Jacob, I. Cohen, and O. Shochet, Phys. Rev. Lett. 75, 1226 (1995).
- [26] F. Jafarpour, T. Biancalani, and N. Goldenfeld, Phys. Rev. Lett. 115, 158101 (2015).
- [27] T. Vicsek and A. Zafeiris, Phys. Rep. **517**, 71 (2012).
- [28] F. Ginelli, Eur. Phys. J. Spec. Top. 225, 2099 (2016).
- [29] H. Chaté, Annu. Rev. Condens. Matter Phys. 11, 189 (2020).
- [30] K. Schakenraad, J. Ernst, W. Pomp, E. H. J. Danen, R. M. H. Merks, T. Schmidt, and L. Giomi, Soft Matter 16, 6328 (2020).
- [31] K. Schakenraad, L. Ravazzano, N. Sarkar, J. A. J. Wondergem, R. M. H. Merks, and L. Giomi, Phys. Rev. E 101, 032602 (2020).
- [32] D. T. Gillespie, J. Comput. Phys. 22, 403 (1976).
- [33] D. T. Gillespie, Annu. Rev. Phys. Chem. 58, 35 (2007).
- [34] I. H. Riedel, K. Kruse, and J. Howard, Science 309, 300 (2005).
- [35] B. M. Friedrich and F. Jülicher, Proc. Natl. Acad. Sci. USA 104, 13256 (2007).
- [36] W. R. DiLuzio, L. Turner, M. Mayer, P. Garstecki, D. B. Weibel, H. C. Berg, and G. M. Whitesides, Nature (London) 435, 1271 (2005).

- [37] E. Lauga, W. R. DiLuzio, G. M. Whitesides, and H. A. Stone, Biophys. J. 90, 400 (2006).
- [38] H. H. Wensink, J. Dunkel, S. Heidenreich, K. Drescher, R. E. Goldstein, H. Löwen, and J. M. Yeomans, Proc. Natl. Acad. Sci. USA 109, 14308 (2012).
- [39] Y. Sumino, K. H. Nagai, Y. Shitaka, D. Tanaka, K. Yoshikawa, H. Chaté, and K. Oiwa, Nature (London) 483, 448 (2012).
- [40] K. Kim, N. Yoshinaga, S. Bhattacharyya, H. Nakazawa, M. Umetsu, and W. Teizer, Soft Matter 14, 3221 (2018).
- [41] M. Loose and T. J. Mitchison, Nat Cell Biol 16, 38 (2014).
- [42] E. L. Meier and E. D. Goley, Curr. Opin. Cell Biol. **26**, 19 (2014).
- [43] B. Liebchen and D. Levis, Phys. Rev. Lett. 119, 058002 (2017).
- [44] J. Denk, L. Huber, E. Reithmann, and E. Frey, Phys. Rev. Lett. **116**, 178301 (2016).
- [45] B. Ventejou, H. Chaté, R. Montagne, and X. Q. Shi, Phys. Rev. Lett. 127, 238001 (2021).
- [46] J. M. Moore, M. A. Glaser, and M. D. Betterton, Soft Matter 17, 4559 (2021).
- [47] A. Chardac, L. A. Hoffmann, Y. Poupart, L. Giomi, and D. Bartolo, Phys. Rev. X 11, 031069 (2021).
- [48] J. Alicea, L. Balents, M. P. A. Fisher, A. Paramekanti, and L. Radzihovsky, Phys. Rev. B 71, 235322 (2005).
- [49] D. J. G. Pearce and L. Giomi, Phys. Rev. E 94, 022612 (2016).
- [50] J. Toner and Y. Tu, Phys. Rev. E 58, 4828 (1998).
- [51] A. Czirók, E. Ben-Jacob, I. Cohen, and T. Vicsek, Phys. Rev. E 54, 1791 (1996).
- [52] G. Grégoire, H. Chaté, and Y. Tu, Phys. Rev. E 64, 011902 (2001).
- [53] D. Nishiguchi, K. H. Nagai, H. Chaté, and M. Sano, Phys. Rev. E 95, 020601(R) (2017).
- [54] V. Holubec, D. Geiss, S. A. M. Loos, K. Kroy, and F. Cichos, Phys. Rev. Lett. 127, 258001 (2021).
- [55] W. Zuo and Y. Wu, Proc. Natl. Acad. Sci. USA 117, 4693 (2020).
- [56] S. Peled, S. D. Ryan, S. Heidenreich, M. Bär, G. Ariel, and A. Be'er, Phys. Rev. E **103**, 032413 (2021).
- [57] A. Jose, G. Ariel, and A. Be'er, Phys. Rev. E **105**, 064404 (2022).
- [58] S. Chatterjee, M. Mangeat, C.-U. Woo, H. Rieger, and J. D. Noh, Phys. Rev. E 107, 024607 (2023).
- [59] P. Buri, Evolution 10, 367 (1956).
- [60] J. H. Gillespie, Population Genetics: A Concise Guide (The Johns Hopkins University Press, Baltimore, 1998).
- [61] E. Mayr, Systematics and the Origin of Species, from the Viewpoint of a Zoologist, 1st ed. (Harvard University Press, Cambridge, 1999).
- [62] W. B. Provine, Genetics 167, 1041 (2004).
- [63] M. Nei, Mol. Biol. Evol. 22, 2318 (2005).
- [64] N. H. Barton, D. E. G. Briggs, J. A. Eisen, D. B. Goldstein, and N. H. Patel, *Evolution* (Cold Spring Harbor Laboratory Press, Cold Spring Harbor, NY, 2007).
- [65] L. L. Cavalli-Sforza, P. Menozzi, and A. Piazza, Science 259, 639 (1993).
- [66] S. F. Elena and R. E. Lenski, Nat. Rev. Genet. 4, 457 (2003).
- [67] S. Ramachandran, O. Deshpande, C. C. Roseman, N. A. Rosenberg, M. W. Feldman, and L. L. Cavalli-Sforza, Proc. Natl. Acad. Sci. USA 102, 15942 (2005).
- [68] O. Hallatschek, P. Hersen, S. Ramanathan, and D. R. Nelson, Proc. Natl. Acad. Sci. USA 104, 19926 (2007).

- [69] M. J. I. Müller, B. I. Neugeboren, D. R. Nelson, and A. W. Murray, Proc. Natl. Acad. Sci. USA 111, 1037 (2014).
- [70] C. D. Nadell, K. Drescher, and K. R. Foster, Nat. Rev. Microbiol. 14, 589 (2016).
- [71] O. Hallatschek, S. S. Datta, K. Drescher, J. Dunkel, J. Elgeti, B. Waclaw, and N. S. Wingreen, Nat. Rev. Phys. **5**, 407 (2023).
- [72] C. Castellano, S. Fortunato, and V. Loreto, Rev. Mod. Phys. **81**, 591 (2009).